nature nanotechnology

Article https://doi.org/10.1038/s41565-023-01360-z

Leaky-wave metasurfaces for integrated photonics

In the format provided by the authors and unedited

Table of Contents

S.1 Recent progress in metasurfaces on waveguides

By incorporating arrays of optical nano-antennas with waveguides, integrated metasurfaces have been developed for conversion between guided and radiation waves, but rarely for generating free-space wavefronts that are extended in two dimensions and with complex profiles. Waveguide-holograms have been proposed long ago as a generalization of grating couplers, but they were based on simple structural units and designed to achieve only amplitude or phase control over the free-space wavefront, while the rich degrees of freedom in optical control offered by metasurfaces remain to be explored.

Table S.1: Summary of work on integrated metasurfaces generating free-space wavefronts

Work	Structural degrees of freedom	Optical degrees of freedom	Optical parameters controlled
Huang *et al. Optica* 6, 119–124 (2019) [5]	1	1	A
Fang *et al. Nanophotonics* **11**, 1923–1930 (2022) [3]	1	1	Φ
Ding *et al. ACS Photonics* **9**, 398–404 (2022) [4]	2	1	Φ
Ha *et al. Advanced Theory and Simulations* **4**, 2000239 (2021) [6]	2	2	Φ_1, Φ_2
Livneh *et al. Optics Express* **30**, 8425–8435 (2022) [7]	2	2	A_1, A_2
This work	4	4	A, Φ, ψ, χ

To achieve full control over the four optical degrees of freedom, at least four structural degrees of freedom are needed in a meta-unit. This has recently been realized in free-space metasurfaces, where each meta-unit was composed of four rectangular meta-atoms with variable lengths and widths [1] or rotation angles [2]. However, limited control over the optical degrees of freedom has been realized in integrated metasurfaces (**Table S.1**). Typically, single phase control [3],[4] or amplitude control [5] was used to manipulate the wavefront generated by an integrated metasurface. By utilizing two structural degrees of freedom in a meta-unit, integrated metasurfaces have been demonstrated to generate distinct free-space wavefronts when guided waves were launched along different directions [6],[7]. In this work, we demonstrate for the first time complete and independent control over the four optical degrees of freedom using an integrated metasurface with four structural degrees of freedom in a meta-unit.

S.2 Perturbed lattice

Here we emphasize that the perturbed lattice of our leaky-wave metasurfaces (LWMs) is *rectangular*, seen in **Fig. S1(a)**, as opposed to *oblique* as in the unperturbed case as well as the example perturbed lattice in **Fig. S1(b)**. This distinction has a meaningful impact on the zone-folding, as seen in **Fig. S1(c)** and **Fig. S1(d)**. These tilings are related by an additional phase factor of π in alternating rows.

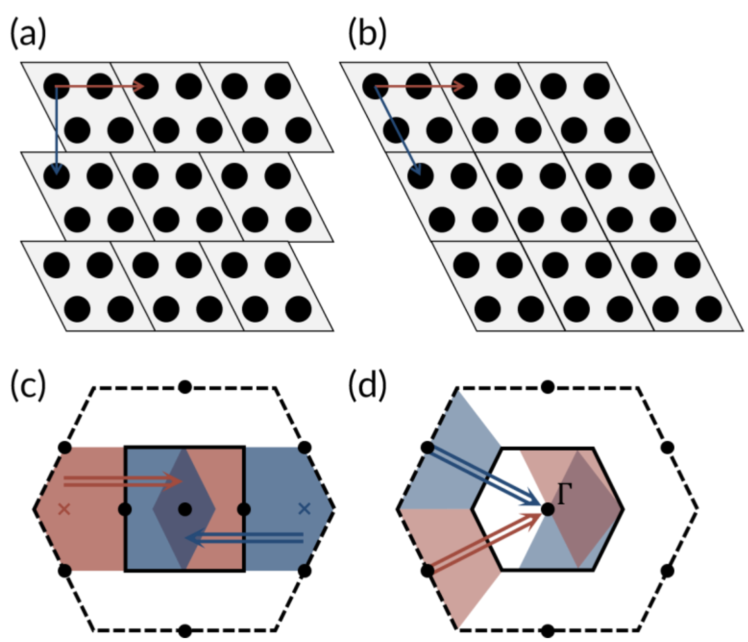

Figure S1. (a) Lattice used in the main text. (b) Alternative tiling of the same unit cells. (c) First Brillouin zone (FBZ) and zone folding for the lattice in (a). (d) FBZ and zone folding for the lattice in (b).

S.3 Spectrally shifting the flat band

Here we show that the unwanted flat band overlapping the Dirac point may be spectrally shifted by manipulating the periodicity of the metasurface lattice in the *x* direction. **Figure S2(a)** shows a lattice with $a_x = 0.35$ μm and $a_y = 0.4$ μm, which is adjusted compared to the lattice used in the main text [**Fig. S2(b)**], where $a_x = a_y = 0.4$ μm. The lattice may be further adjusted to have $a_x = 0.45$ μm [**Fig. S2(c)**]. The band diagrams of the three cases are provided in **Figs. S2(d-f)**, showing that the flat band redshifts with increasing value of a_x, and that it is degenerate with the Dirac point when $a_x = a_y$. The shrunken lattice in **Fig. S2(a)** is a good option for blueshifting the flat band out of the spectral region of interest, avoiding any potential complications entirely.

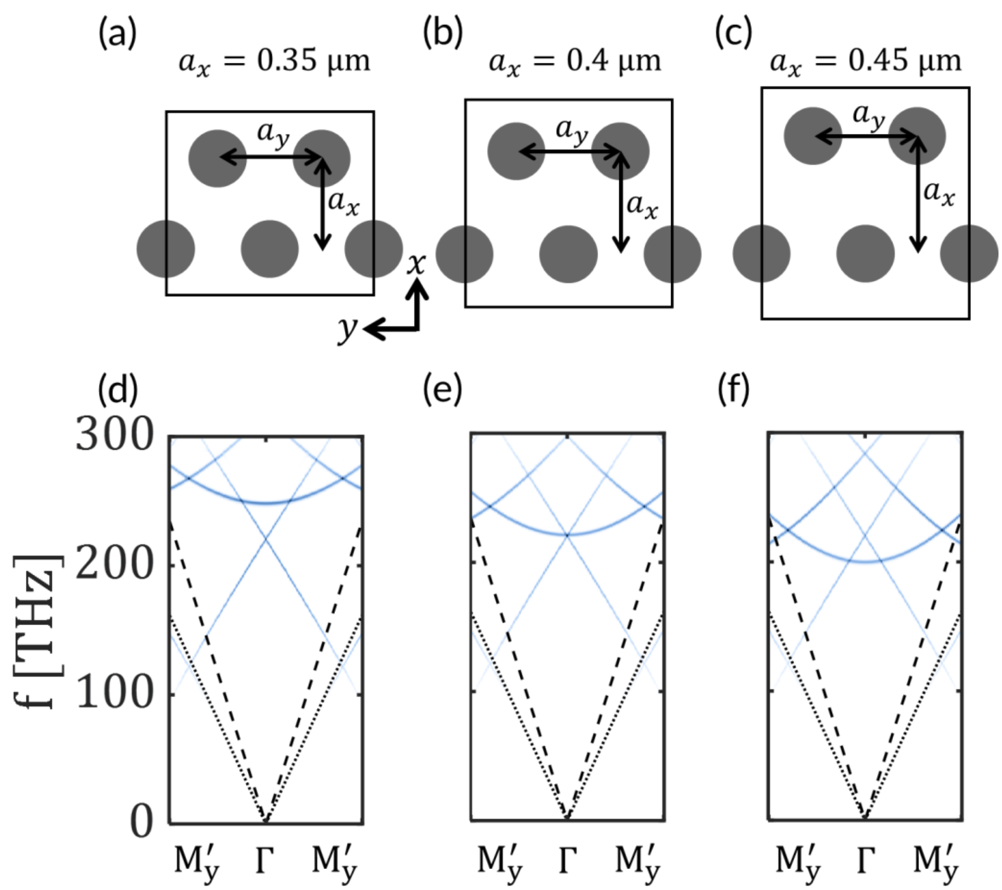

Figure S2. (a-c) Lattices with varying values of a_x but fixed value of $a_y = 0.4$ μm. (d-f) The band diagrams of the period-doubled lattices in (a-c), showing that the flat band is tuned by the lattice parameter a_x, while the Dirac point is minimally affected.

S.4 Integrity of the Dirac point for example meta-units

While in the previous section the band diagrams were computed based on unperturbed structures, here we study the impact of perturbations on the band diagrams. In particular, for the shrunken lattice of **Fig. S2(a)**, we explore five example meta-unit geometries. We do so for two device architectures, including the one in the main text based on silicon nitride and polymer [**Fig. S3(a)**] and another common integrated photonics platform based on silicon-on-insulator wafers [**Fig. S3(b)**]. The five example meta-units are depicted in **Fig. S3(c)**, including various high and low symmetry cases. From left to right, the parameters used are:

1. $(\delta_1, \delta_2, \alpha_1, \alpha_2) = (0.06\ \mu\text{m}, 0.06\ \mu\text{m}, 0°, 0°)$
2. $(\delta_1, \delta_2, \alpha_1, \alpha_2) = (0.06\ \mu\text{m}, 0, 0°, 0°)$
3. $(\delta_1, \delta_2, \alpha_1, \alpha_2) = (0.06\ \mu\text{m}, 0.06\ \mu\text{m}, 45°, 45°)$
4. $(\delta_1, \delta_2, \alpha_1, \alpha_2) = (0.06\ \mu\text{m}, 0.06\ \mu\text{m}, 0°, 45°)$
5. $(\delta_1, \delta_2, \alpha_1, \alpha_2) = (0.06\ \mu\text{m}, 0.035\ \mu\text{m}, -15°, 52°)$

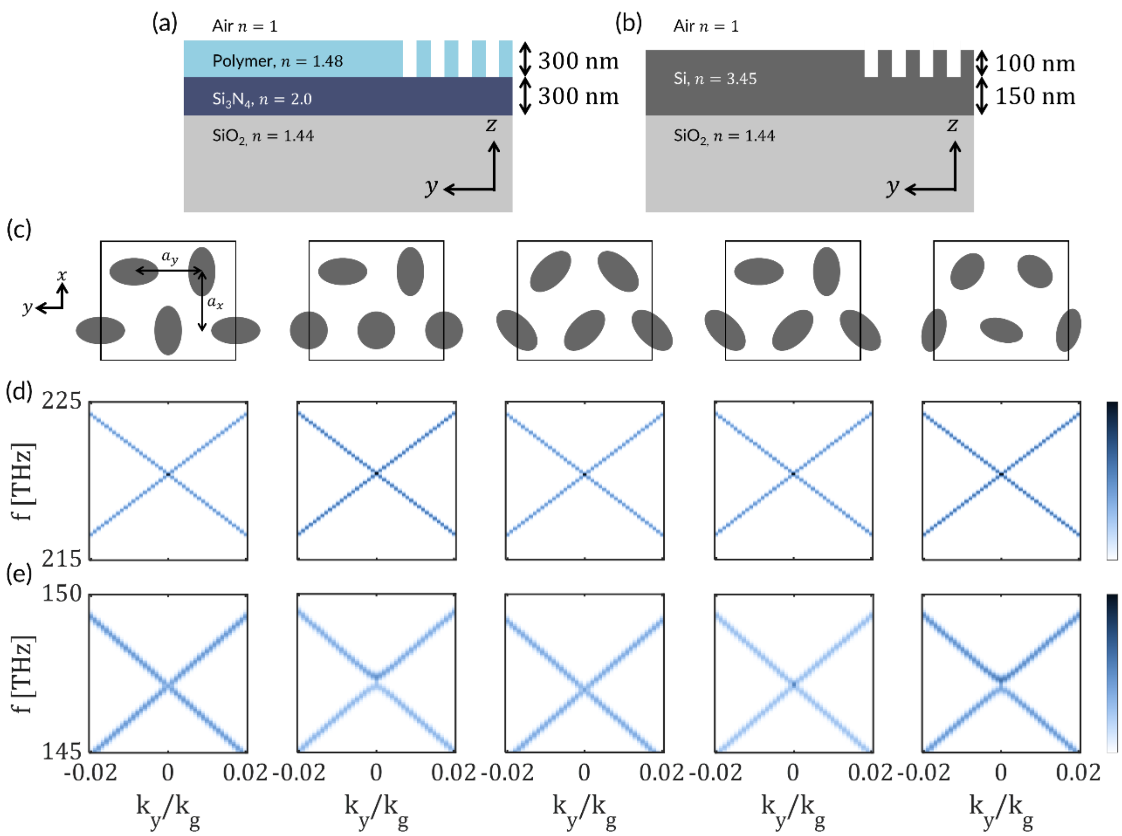

Figure S3. (a,b) Two example system architectures used to study the integrity of the Dirac point near broadside. (c) Five meta-units explored. (d) Band diagrams of the five meta-units for the architecture in (a). (e) Band diagrams of the five meta-units for the architecture in (b). $k_g = \pi/a_y$ is the magnitude of a reciprocal lattice vector in the unperturbed lattice.

As seen in **Fig. S3(d)**, the architecture of the main text [**Fig. S3(a)**] shows negligible impact of meta-unit geometry on the dispersion. The range of k-space here corresponds to roughly $\pm 2°$ at the central operating frequency, chosen due to its relevance to the angular resolution of the devices in the main text. For instance, the focusing LWM in **Fig. 5** of the main text has a numerical aperture corresponding to $\pm 5.7°$, and is frequency tuned across an angular range of about $-1°$ to $3.5°$.

However, as seen in **Fig. S3(e)**, in the higher contrast system [**Fig. S3(b)**], observable (but small) stopgaps are present in the low symmetry cases. The range of k-space here corresponds to roughly $\pm 2.92°$. These results indicate that the devices of the main text should be expected to operate continuously as a function of frequency, but that this assumption begins to break down as the index contrast increases and degree of symmetry decreases. For the high-index-contrast system, operating directly at the crossing frequency may induce in-plane back reflection and other forms of unwanted in-plane scattering of the mode, impacting the fidelity of the leaky wave.

Relatedly, it is notable that the dispersion diagrams in the low-index-contrast case are effectively unchanged by the choice of meta-unit. This suggests that the in-plane guided mode's phase evolution is invariant to the scattering profile of choice, simplifying the design procedure. However, small but noticeable frequency shifts are observed in the high-index-contrast system. To mitigate these effects, a more complex meta-unit library that varies the average dimensions of the geometric features should be used, in order to redshift or blueshift the dispersion as needed.

S.5 Schematic derivation of the selection rules

The principles behind the control over out-coupled radiation in this work are rooted in the symmetry properties of quasi-bound states in the continuum (q-BICs). These long-lived states are governed by selection rules, which specify whether symmetry considerations allow the state to be excited. While this was systematically carried out in Ref. [8] in the language of group theory, a simpler schematic approach may also clarify which polarized out-coupled radiation—if any—is supported by a q-BIC due to a certain symmetry-lowering perturbation. Here, we briefly describe the process and demonstrate it for several example meta-units.

The process of schematically deriving the selection rules involves looking at the out-of-plane field component, which in the main text is the electric field E_z (we employ a TM mode). As shown in Ref. [8], the group theory approach is equivalent to treating the out-of-plane field components as "charges" and writing down the distribution of in-plane "moments" connecting them. If there is a net dipole moment, out-coupled light with the corresponding polarization will be produced in the surface normal direction (broadside emission). If there is no net moment, the mode is bound. If there is only a higher-order moment (e.g., a quadrupole), the q-BIC may leak but only to off-normal angles (and generally, extremely inefficiently). If there is both a dipole and a quadrupole, the dipolar contribution dominates to first order (it is the leading-order term), especially near broadside. By construction, the q-BICs we are interested in are *bound* in the absence of a perturbation. That is, the arrangement of "charges" is highly symmetric (and subwavelength in spacing), containing no net in-plane dipole moment. For this reason, we consider only the additional "charges" *induced by the perturbation*, and determine if these produce a net moment. We may otherwise ignore the unperturbed field components, because they do not directly contribute to the out-of-plane scattering. The result of this process is to find the electric-field components E_x and E_y for the out-coupled field $E_{out} = [E_x \quad E_y]^T$. For TE modes, the procedure is identical, but the field component H_z of a q-BIC is studied to determine the out-coupled *magnetic* field $H_{out} = [H_x \quad H_y]^T$. Since in free space the electric-field and magnetic-field components are orthogonal, TE and TM modes in our system must out-couple to orthogonal polarizations. For this reason, it is sufficient to write down one set of selection rules (we choose TM modes). Finally, one departure from Ref. [8] is that here we must apply this procedure to *traveling* waves, rather than standing waves. To apply the same approach, we break the traveling wave down into its real and imaginary components, *each of which is a standing wave*. For this reason, we must independently assess the selection rules for the real and imaginary components of the traveling wave.

In **Fig. S4**, six example meta-units with different choices of $(\delta_1, \delta_2, \alpha_1, \alpha_2)$ are depicted. We distinguish between the real part of the traveling wave (top row in each sub-figure) and imaginary part of the traveling wave (bottom row in each sub-figure), and further between the first perturbation (light blue ellipses) and second perturbation (dark gray ellipses). To determine the "charges" induced by each perturbation, we remember that our system is an array of *holes*. That is, when a circle is made into an ellipse, the expanded diameter of the hole *takes away* high-index material compared to the unperturbed lattice, meaning that the affected standing-wave lobe's field strength decreases. This makes a positive lobe *less positive*, written down as a negative charge, and similarly, makes a negative lobe *less negative*, written down as a positive charge. Likewise, where an ellipse has been created by contracting a circle, we have *added* high-index material, making a positive lobe *more positive* (positive charge) and a negative lobe *more negative* (negative charge). We write down the charges in this way for each perturbation and each lobe of the real and imaginary components, and then see, for each perturbation, if there is a net dipole moment.

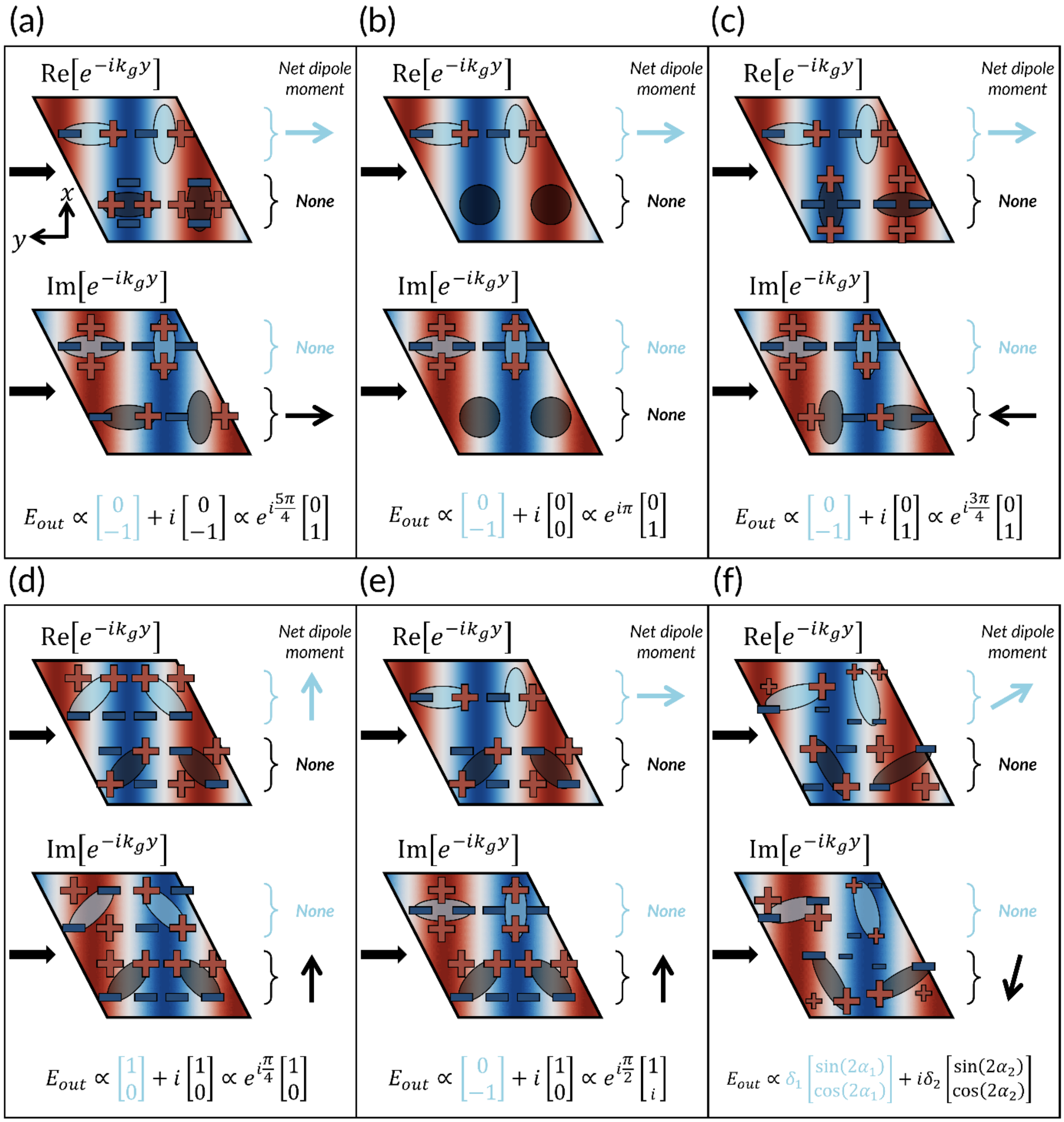

Figure S4. Example schematic derivations of the selection rules. (a) Device with $(\delta_1, \delta_2, \alpha_1, \alpha_2) = (d, d, 0°, 0°)$, where d is some constant. (b) Device with $(\delta_1, \delta_2, \alpha_1, \alpha_2) = (d, 0, 0°, 0°)$. (c) Device with $(\delta_1, \delta_2, \alpha_1, \alpha_2) = (d, -d, 0°, 0°)$, or equivalently, $(\delta_1, \delta_2, \alpha_1, \alpha_2) = (d, d, 0°, 90°)$. (d) Device with $(\delta_1, \delta_2, \alpha_1, \alpha_2) = (d, d, 45°, 45°)$. (e) Device with $(\delta_1, \delta_2, \alpha_1, \alpha_2) = (d_1, d_2, 0°, 45°)$. (f) Device with some general choice of $(\delta_1, \delta_2, \alpha_1, \alpha_2)$.

In the first example, **Fig. S4(a)**, we see that the first perturbation induces a net dipole moment pointing in the negative y direction for the real part of the field, but induces a quadrupole moment for the imaginary part of the field. Similarly, the second perturbation induces a quadrupole moment for the real part but a net dipole moment in the negative y direction for the imaginary component. Both components produce only y-oriented dipole moments, meaning that the scattered field is y-polarized. The real and imaginary components have the same magnitude and sign (negative), meaning that the superposition of the two yields a phase of $5\pi/4$ (third quadrant of the complex space). In comparison, **Fig. S4(b)** removes Perturbation 2, leaving only the single moment, corresponding to a phase of π, while **Fig. S4(c)** reverses the sign of Perturbation 2 compared to **Fig. S4(a)**, yielding a phase of $3\pi/4$ (second quadrant). This phase coverage continues over 2π for the various iterations of signs and relative magnitudes of the two perturbations, as depicted in **Fig. 3(c)** of the main text. This phase is a classic geometric phase: upon making a closed contour that encircles a singularity in this parameter space, we have accumulated 2π in phase. As shown in Ref. [9], here the phase is polarization agnostic, as it may apply to any desired polarization.

Next, **Fig. S4(d)** depicts the perturbations oriented at 45° angles, which induces a net dipole moment in the transverse direction, x. A similar set of meta-units to **Figs. S4(a-c)** could be drawn for this orientation of meta-units, and a similar geometric phase encircling the origin in **Fig. 3(c)** of the main text is observable for this polarization. More generally, at perturbation orientation angles between 0° and 45°, custom linear polarizations with amplitude and phase control are possible.

Moving away from linear polarizations, **Fig. S4(e)** shows Perturbation 1 oriented at an angle $\alpha_1 = 0°$ but Perturbation 2 having $\alpha_2 = 45°$. In this case, the real part scatters to a $-y$-oriented moment, while the imaginary component scatters to a $+x$-oriented moment, yielding circular polarized light if the magnitudes of the moments are the same (tuned by adjusting both perturbation strengths $\delta_1 = d_1$ and $\delta_2 = d_2$). Adding 90° to either perturbation (but not both) reverses the handedness of circular polarization emitted. And rotating the "basis" of linear polarizations from $-y$

and $+x$ to another coordinate system, $-y'$ and $+x'$, controls a geometric phase [as depicted along the black dashed contours in **Figs. 3(e,f)** of the main text]. Most generally, **Fig. S4(f)** shows an arbitrary perturbation, producing a custom magnitude and orientation of the real part and a second custom magnitude and orientation of the imaginary part of the field, which superpose to a custom elliptical state with designer amplitude and phase.

S.6 Simulations of meta-unit responses excited by TE and TM modes

Figure S5 shows FDTD simulation results validating that the Jones vector response of a half meta-unit composed of one pair of ellipses and excited by a TM slab waveguide mode can be modeled as

$$\begin{pmatrix} E_x \\ E_y \end{pmatrix} = \delta \begin{pmatrix} a_x \sin 2\alpha \\ a_y \cos 2\alpha \end{pmatrix}, \tag{1}$$

whereas the response of a half meta-unit excited by a TE slab waveguide mode can be modeled as

$$\begin{pmatrix} E_x \\ E_y \end{pmatrix} = \delta \begin{pmatrix} a_x \cos 2\alpha \\ a_y \sin 2\alpha \end{pmatrix} + \begin{pmatrix} c_x \\ 0 \end{pmatrix}. \tag{2}$$

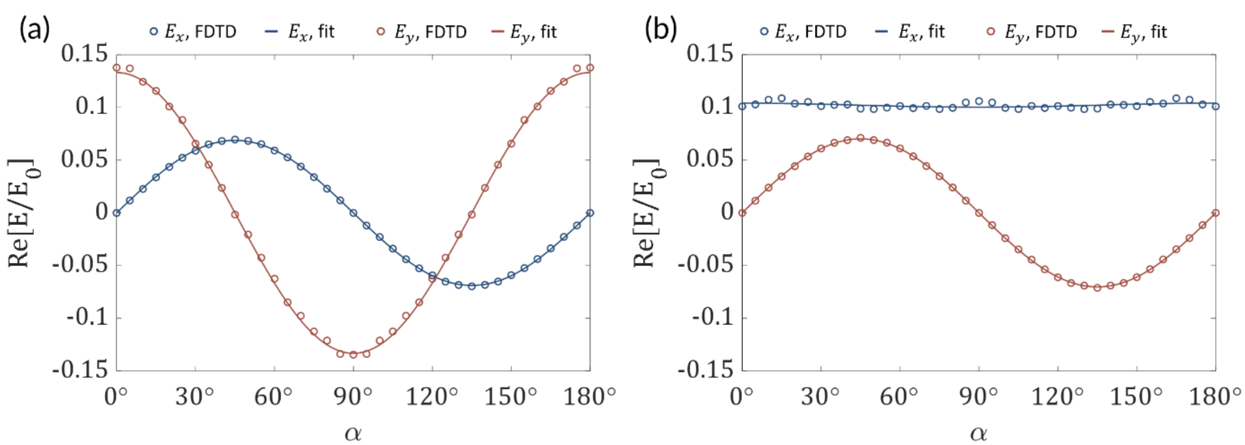

Figure S5. Full-wave simulations showing the responses of a half meta-unit excited (a) TM and (b) TE slab waveguide modes. The E_x component of surface emission excited by a TE slab waveguide mode [blue in (b)] contains a large DC and relatively small AC component; the latter drastically increases when the degree of asymmetry in the z direction is reduced (refractive-index contrast between the substrate and superstrate of the device is reduced).

Next, we study these responses as a function of the in-plane incident angle of the TM guided mode. **Figure S6** shows a comparison of the responses at an incident angle of $\theta = 0$ (along the $-y$

direction) and those at $\theta = 4.8°$. The latter is approximately twice the maximum deviation of the local propagation direction of the guided wave from the $-y$ direction, which occurs at the edges of the tapered slab waveguide. The results show that there is minimal difference in the meta-unit responses.

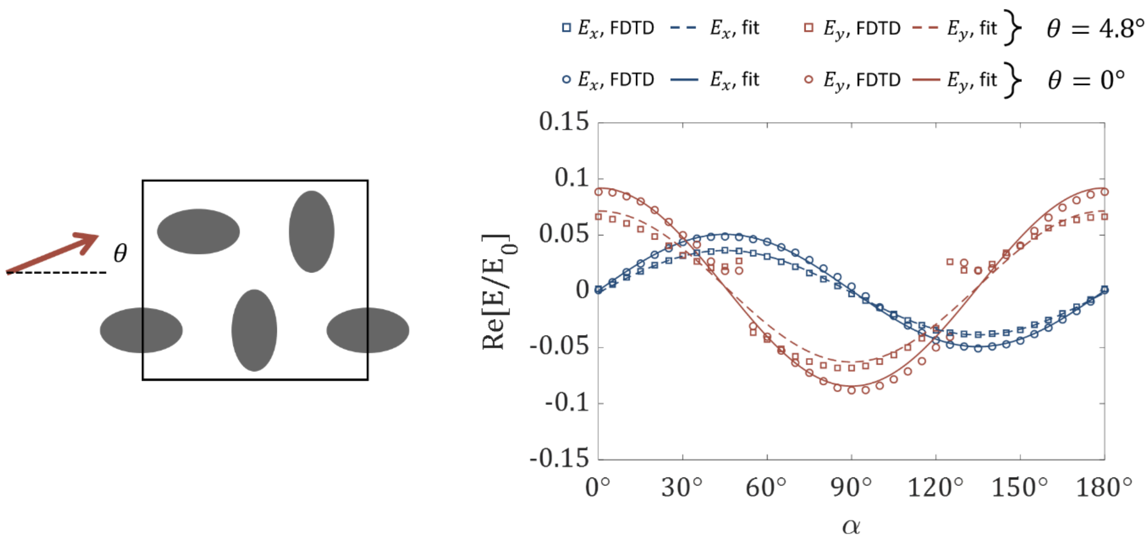

Figure S6. Full-wave simulations comparing the meta-unit responses at two incident angles of the TM guided mode.

Finally, for the TM case, **Fig. S7** shows the Q-factor of a meta-unit (with periodic boundary conditions) as a function of perturbation strength δ_1 (δ_2 set to zero), exhibiting the defining scalar law for q-BICs [10]

$$Q = \frac{C}{\delta_1^2}, \tag{3}$$

where $C = 950\mu m^2$ is retrieved.

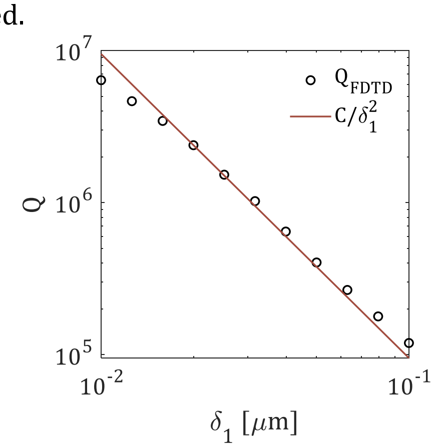

Figure S7. Full-wave simulations of the Q-factor as a function of perturbation strength.

S.7 Polarization-resolved measurements

Here we report corroborating experiments demonstrating that the phase-amplitude LWM devices emit linearly polarized light. **Figures S8(a-e)** depict measurement results taken with a polarization analyzer in front of the infrared camera to confirm that the surface emission of the focusing LWM in the main text [**Figs. 5(a-e)**] is linearly polarized along the y direction. **Figures S8(f-j)** depict the same but for a device designed to focus surface emission polarized in the x direction. Note that this device is an amplitude-only implementation, following the design of a continuous Fresnel zone plate [**Fig. S8(f)**].

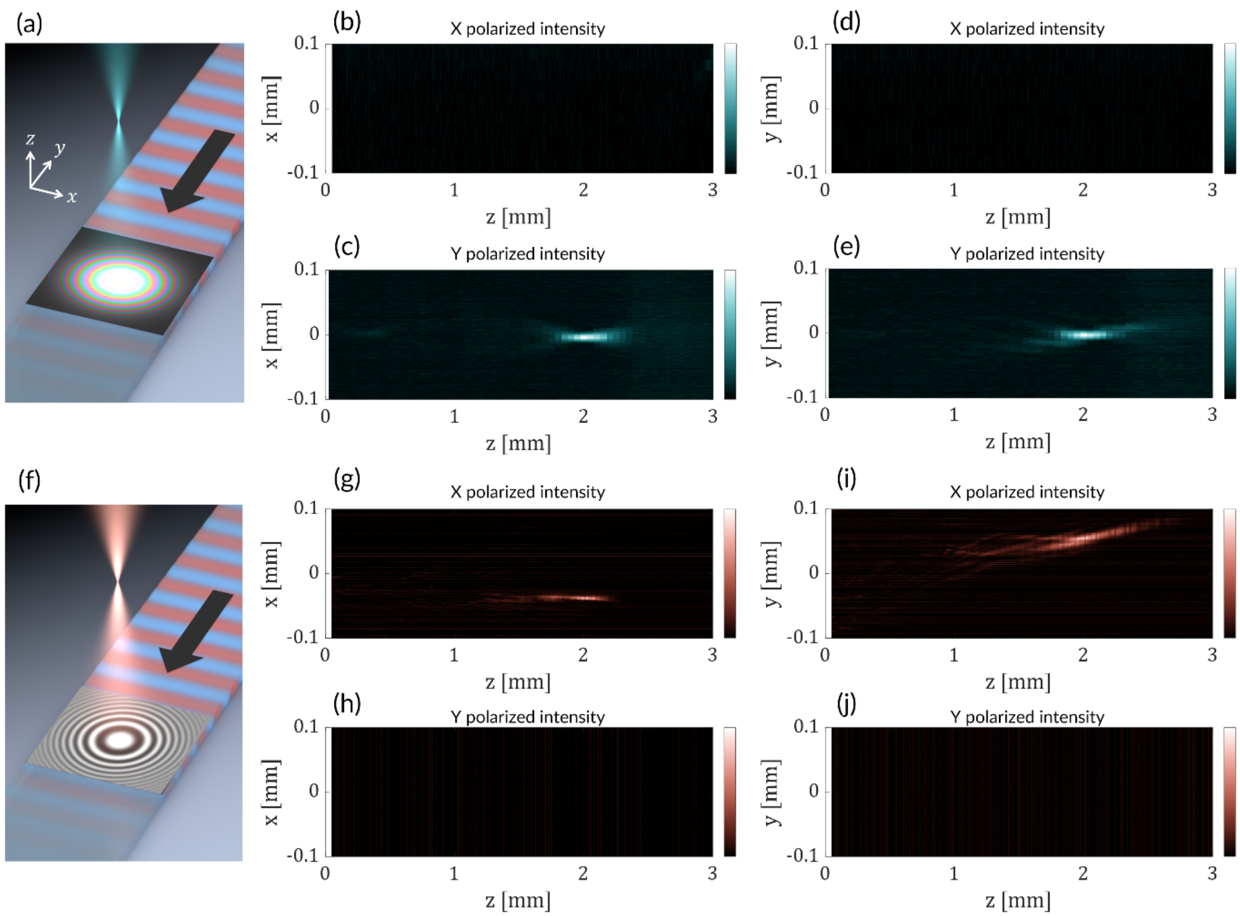

Figure S8. (a) Schematic of a LWM producing a focusing beam that is y-polarized. (b) and (c) Measured intensity distributions on the xz plane through a polarization analyzer oriented along the x (b) and y (c) direction. (d) and (e) Measured intensity distributions on the yz plane through the polarization analyzer oriented along the x (d) and y (e) direction. Data were taken using the same integration times at $\lambda_0 = 1530$ nm and plotted on the same color scale. (f-j) Same as (a-e) but for a

Fresnel zone LWM designed to focus x-polarized surface emission. Data were taken using the same integration times at $\lambda_0 = 1620$ nm and plotted on the same color scale.

Next, we report a LWM designed to produce surface emission in the form of a radially polarized beam. The measured intensity profiles $I_p(x, y)$ at the LWM plane while varying the orientation θ_p of a polarization analyzer are shown in **Fig. S9**. To quantify the measured responses, we consider the theoretical intensity distribution for a radially polarized device as a function of the theoretical polarizer orientation angle θ_{theo}:

$$I_{theo}(x,y) = \cos^2\left[\theta(x,y) - \theta_{theo}\right] = \frac{1+\cos\left[2\theta(x,y) - 2\theta_{theo}\right]}{2}, \tag{4}$$

where the azimuthal angle $\theta(x, y) = \arctan\,(y/x)$. For each experimental θ_p, we compute an overlap integral of the experimental profile $I_p(x, y)$ and the theoretical profile for various values of θ_{theo}:

$$\eta = \frac{\iint dxdy I_p(x,y)\cos\left[2\theta(x,y) - 2\theta_{theo}\right]}{\frac{1}{2}\iint dxdy\cos^2\left[2\theta(x,y) - 2\theta_{theo}\right]}. \tag{5}$$

Then, for each θ_p we find the best-fit θ_{theo} that maximize η, and call it θ_{max}. The results are shown in the central panel of **Fig. S9**. The capability to produce a radially polarized beam demonstrates complete control over linear polarization in a single device.

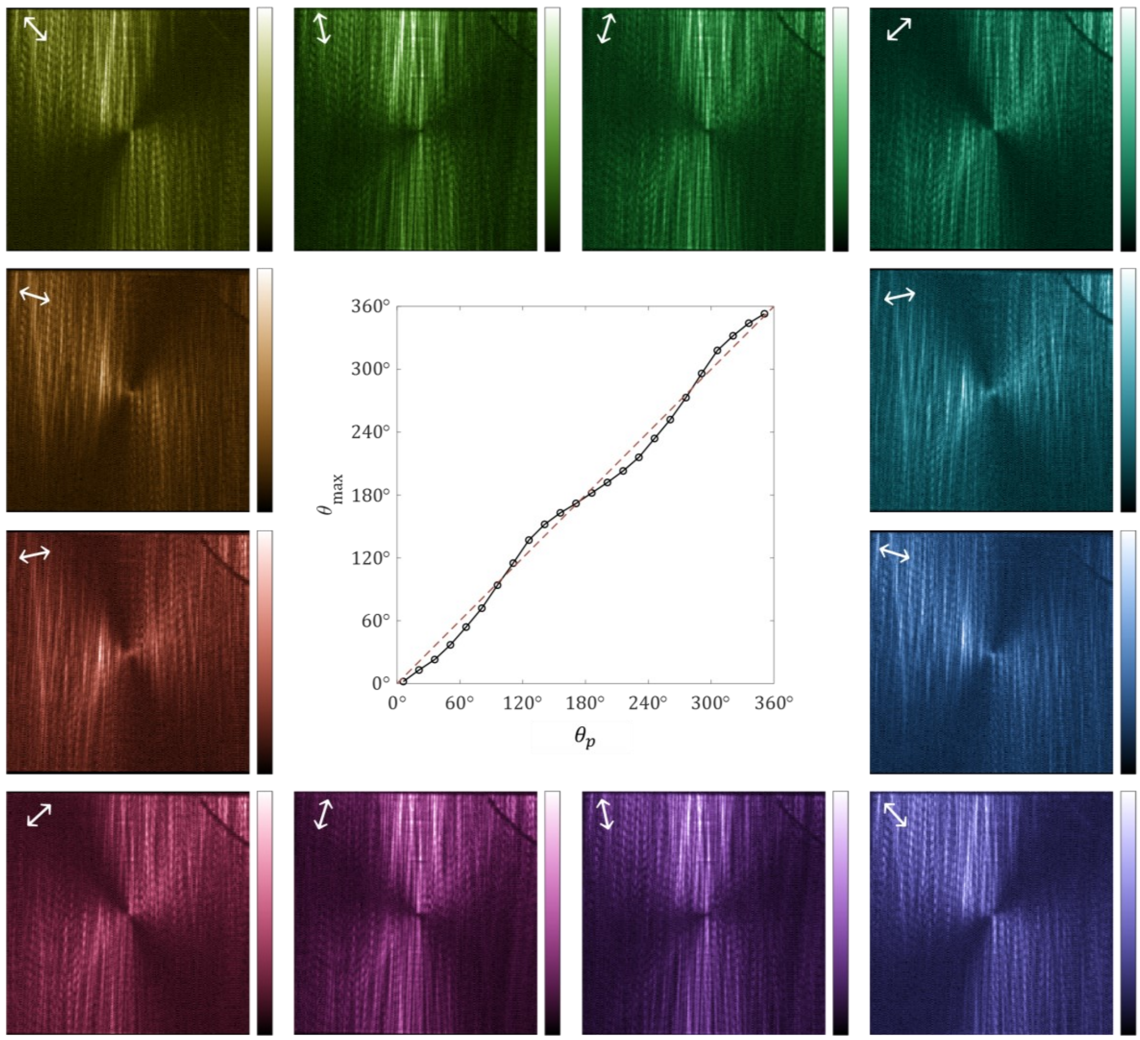

Figure S9. Border panels: Measured intensity profiles at the LWM plane while varying the orientation θ_p of a polarization analyzer. Center panel: Computed best-fit angle θ_{max} for each experiment θ_p, showing excellent agreement with the ideal case (dashed line).

S.8 Additional experimental devices

Here we report three additional experimentally demonstrated devices, including a two-image hologram producing x-polarized holographic images [**Figs. S10(a-c)**], a vortex beam generator with orbital angular momentum (OAM) $\ell = 1$ [**Figs. S10(d-f)**], and a phase-only Kagome lattice generator [**Figs. S10(g,h)**]. The first device demonstrates that surface emission from LWMs can be x-polarized (by choosing perturbation orientation angles $\alpha_1 = \alpha_2 = 45°$). The second device further evidences the customizability of LWMs as a platform for free-space communications using OAM. The third device has only phase control over the device plane, utilizing more of the incident power to generate a Kagome lattice (the optical phase across the spots in the Kagome lattice, however, is not uniform, while the spots produced by the phase-amplitude Kagome lattice generator in the main text share the same phase).

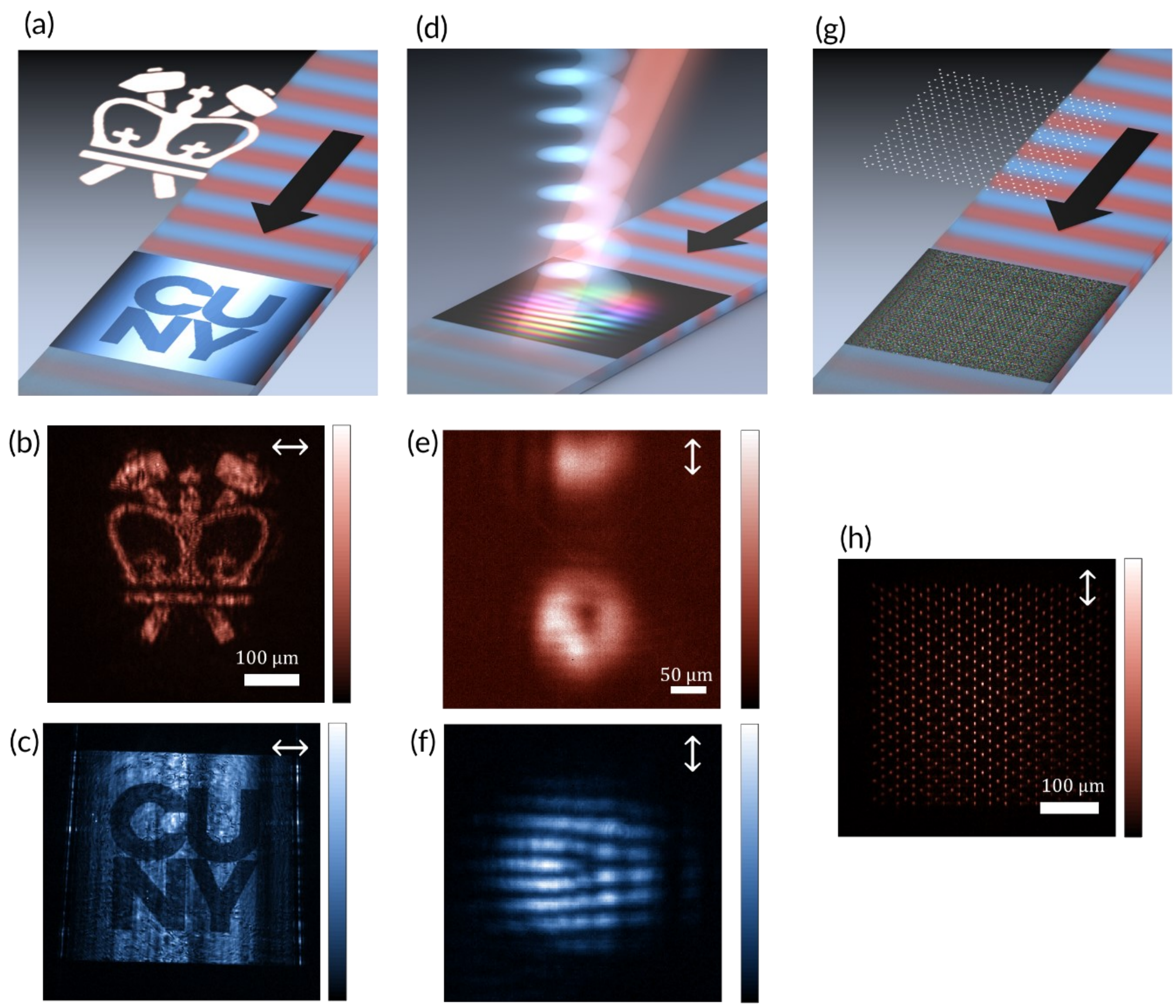

Figure S10. (a) Schematic of a two-image hologram that produces x-polarized holographic images. (b) Measured holographic image (Columbia Engineering Logo) at a plane $z = 1$ mm away from the LWM. (c) Measured gray-scale image (CUNY logo) at the LWM plane. (d) Schematic of a LWM producing an OAM beam with $\ell = 1$, along with a tilted Gaussian beam as a reference. (e) Measured surface emission of the device at a plane $z = 10$ mm away from the LWM, where the OAM and Gaussian beams are separated. (f) Measured interference of the two beams at $z = 1.65$ mm, showing a characteristic forked pattern. (g) Schematic of a phase-only Kagome lattice generator. (h) Measured Kagome lattice at a plane $z = 0.5$ mm away from the LWM.

S.9 Details of devices shown in the main text

We report the details of the amplitude, phase, and polarization profiles, as well as the profiles of device geometric parameters, for the devices in the main text. In each box below (black solid lines), we report the target fields [i.e., near-fields immediately above the metasurface, in terms of (A, Φ, ψ, χ)], mode-corrected field profiles [i.e., fields corrected by the intrinsic amplitude and phase profiles of the waveguide mode, in terms of (A, Φ, ψ, χ)], and device geometry [i.e., perturbation parameters across the device, in terms of $(\delta_1, \delta_2, \alpha_1, \alpha_2)$]. For the linearly polarized devices, the values of the perturbation orientation angles are fixed to be $\alpha_1 = \alpha_2 = 0°$, except for **Fig. 5(n)** (x-polarized surface emission), in which case we set $\alpha_1 = \alpha_2 = 45°$. Each box is labeled with the sub-figure of the corresponding device schematic in the main text.

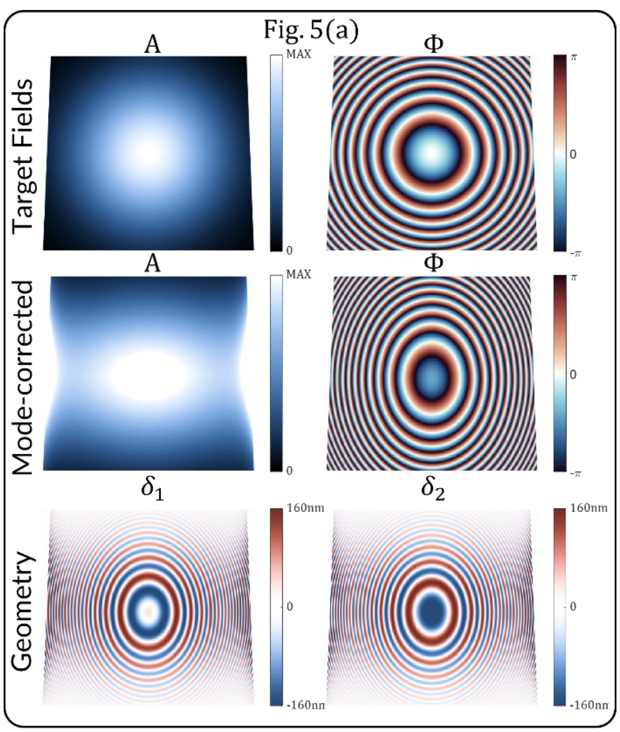

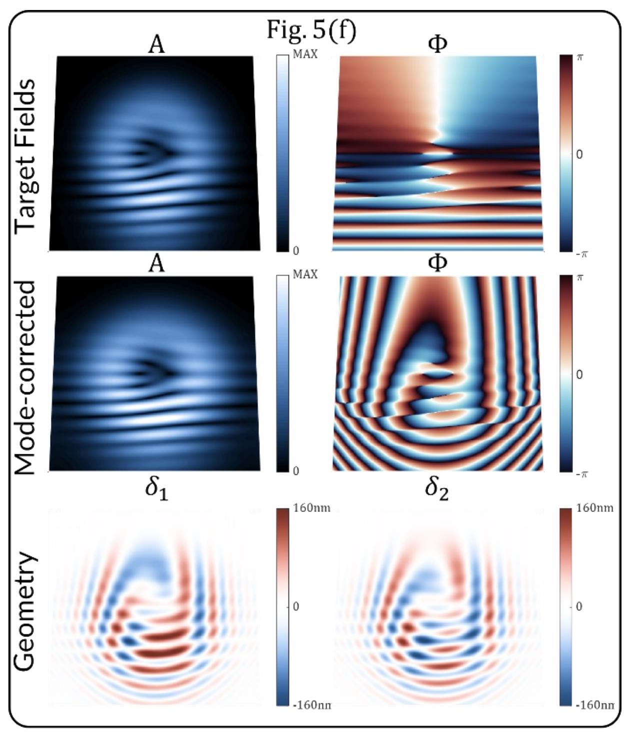

Fig. 5(j)

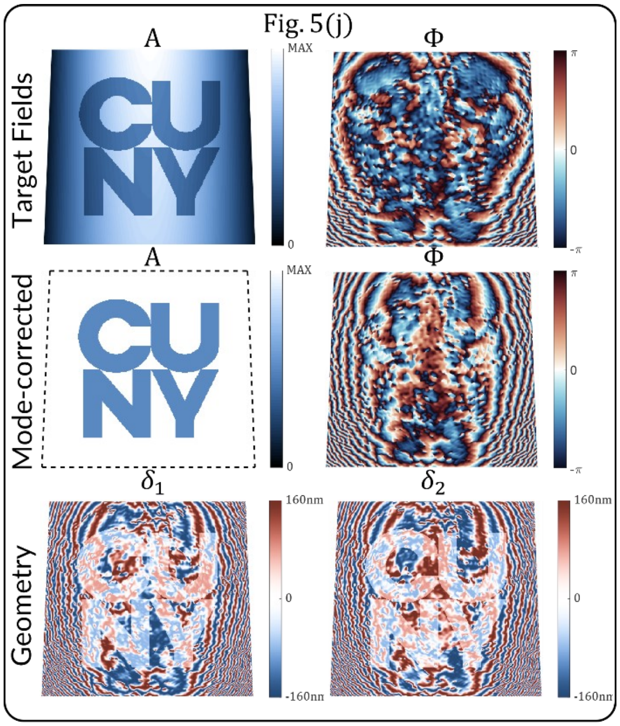

Fig. 5(n)

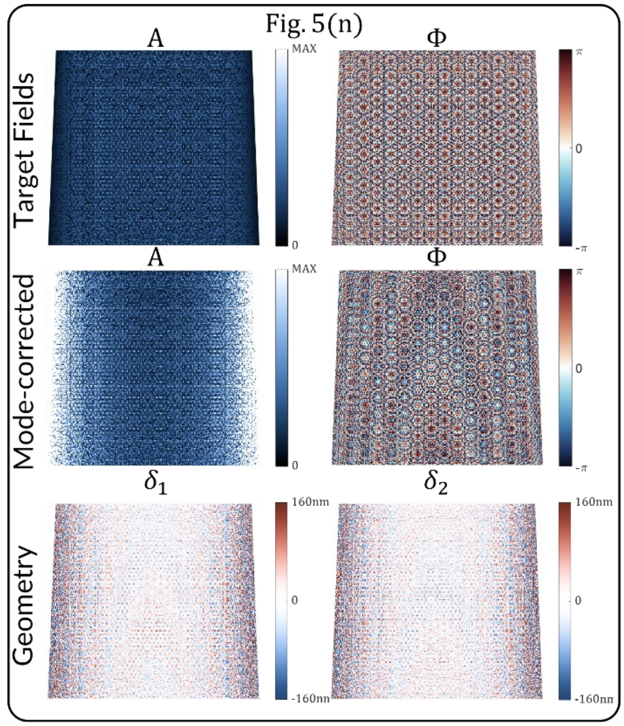

Fig. 6(a)

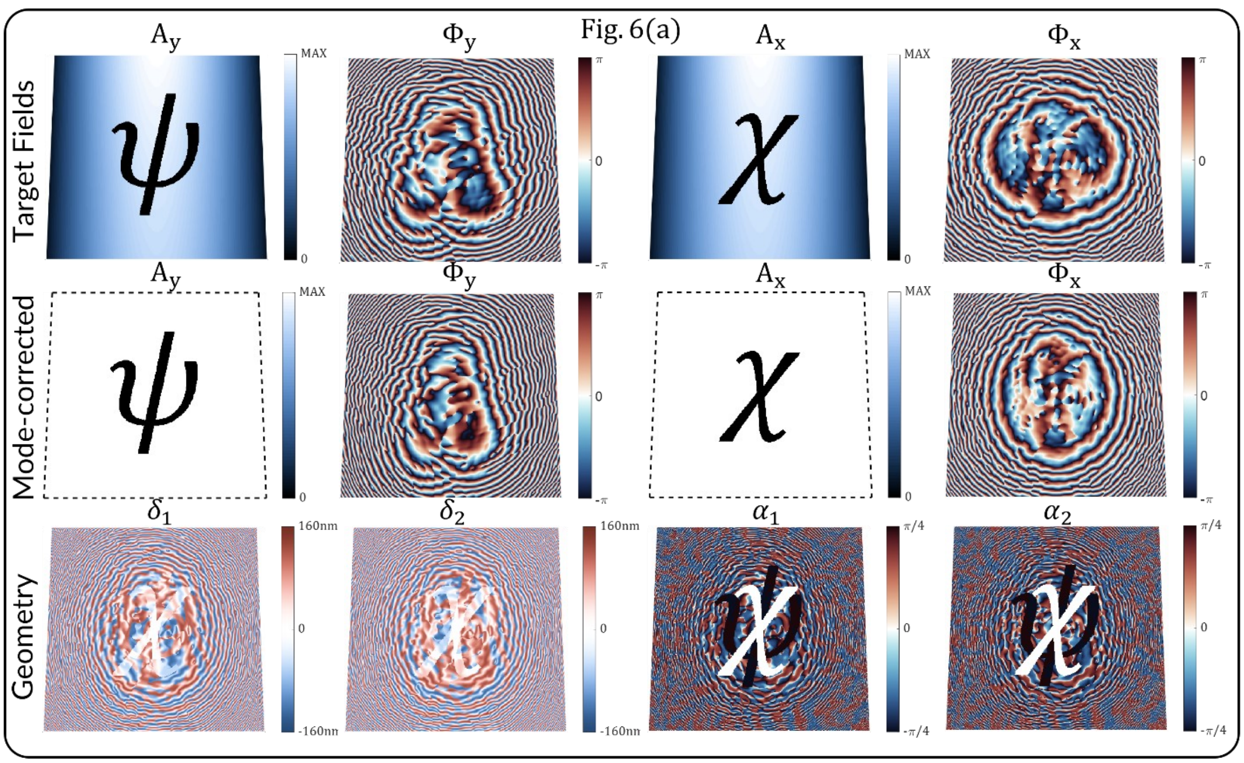

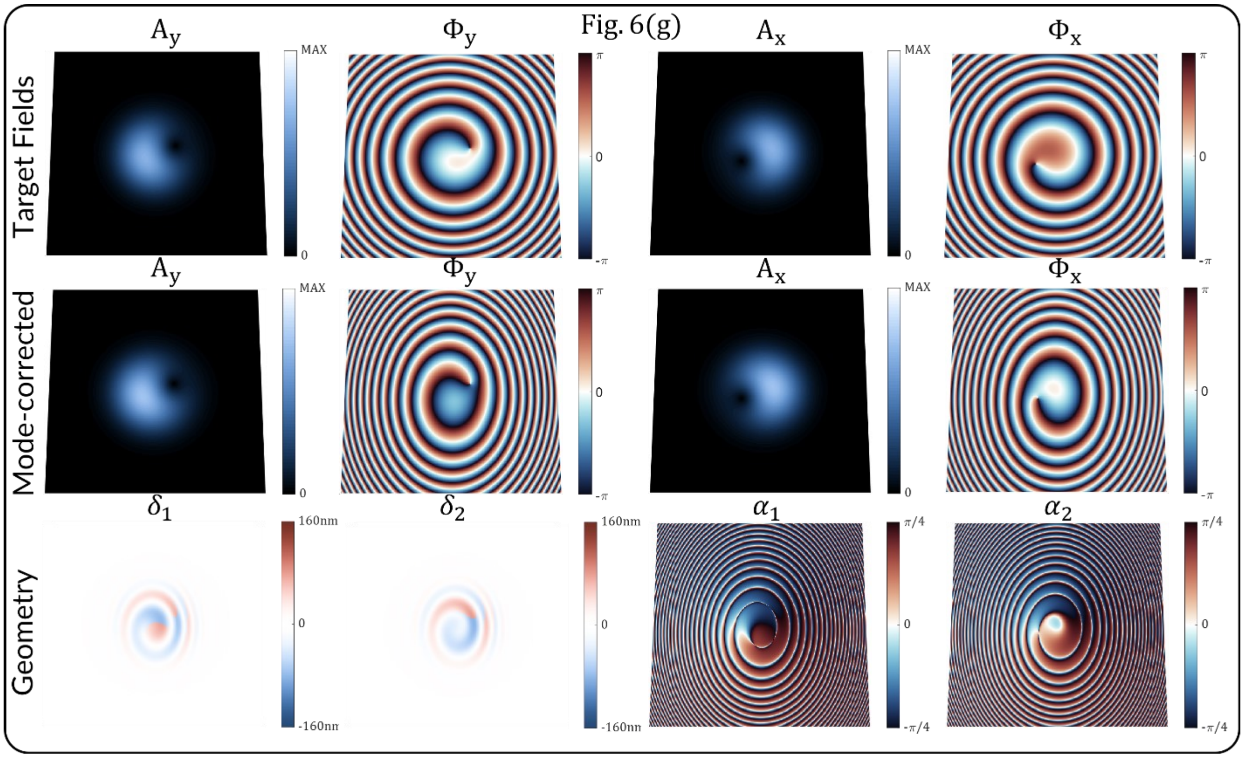

S.10 Example evolution of optical intensity profiles

Figure S11 depicts the evolution of transverse optical intensity distributions for the two-image hologram, vortex beam generator, and four-image holograms in the main text. The data for the holograms are shown between the LWM plane ($z = 0$ mm) and the holographic plane ($z = 1$ mm), while the data for the vortex beam generator are shown between $z = 0$ mm and $z = 8$ mm.

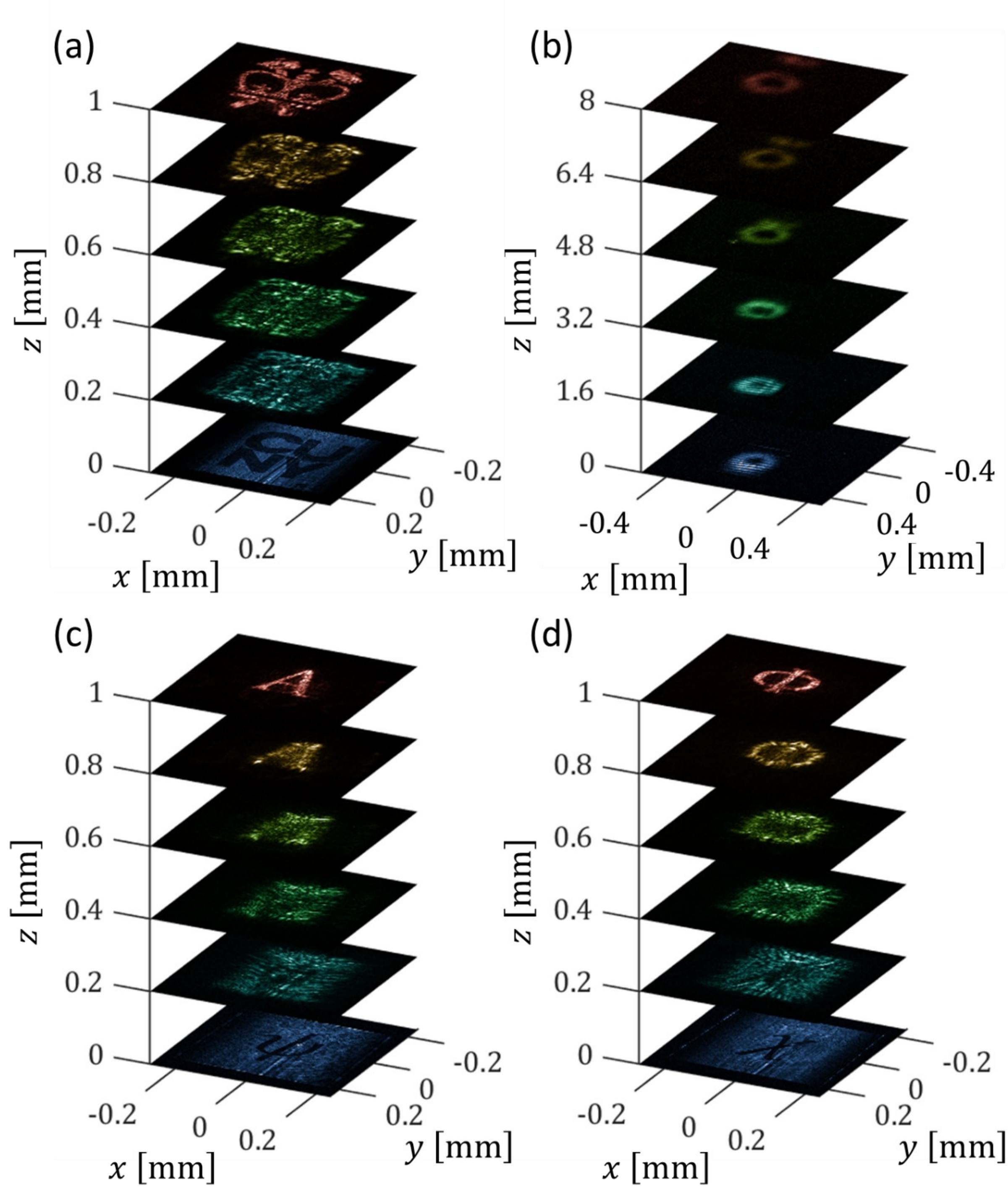

Figure S11. (a) Experimental optical intensity distributions of the two-image hologram at six cross-sectional planes. (b) Experimental optical intensity distributions of the vortex beam generator at six cross-sectional planes. (c) Experimental optical intensity distributions of the four-image hologram at six cross-sectional planes, for y-polarized light. (d) Experimental optical intensity distributions of the four-image hologram at six cross-sectional planes, for x-polarized light.

S.11 Optimizing radiation efficiency

While in the main text we limit ourselves to the simple case in which most of the optical power remains in the device plane after a single pass through the LWM, here we briefly discuss design strategies for optimizing the device radiation efficiency. In this section, we limit the discussion to devices with target outgoing amplitude envelopes that are varying along the in-plane propagation direction (y) but are *invariant* along the transverse in-plane direction (x). The next section discusses further complications in the more general case of 2D amplitude profiles.

Adjusting the approach in Ref. [11], we describe the leakage from a LWM by two equations. First, the complex amplitude $A(y)$ of a guided mode decaying in a LWM with constant and small perturbation follows:

$$\frac{d\left|A(y)\right|}{dy} = -\alpha\left|A(y)\right|, \tag{6}$$

while the out-coupled light's complex amplitude $B(y)$ follows:

$$B(y) = \beta A(y). \tag{7}$$

Here, α is the leakage rate controlled through the magnitude of the perturbation, and β is a complex quantity determining the amplitude and phase of the out-coupled field. Note that for a polarization-manipulating LWM, B and β are vectors in some polarization basis. Likewise, one may separate the out-coupled light into the upper and lower half spaces, e.g., having two copies of Eqn. (7) with B_{up} and B_{down}, respectively. Here, for simplicity in exploring the strategies for fully out-coupling the guided mode, we consider a scalar field scattered to a single half space.

In the case of q-BICs, we may explicitly relate α and β to the perturbation. For a travelling q-BIC having a linear dispersion relation and an optical lifetime $\tau = Q/\omega_0$ for a Q-factor Q and resonant frequency ω_0, we expect that a leaky wave has a characteristic propagation length of $v_g \tau = 1/(2\alpha)$. The group velocity $v_g = c_0 / n_{eff}$, where c_0 is the speed of light in vacuum and $n_{eff} = \lambda_0 / P$ is the guided mode's effective modal index, can also be written as $v_g = \omega_0 / k_g$, where $k_g = 2\pi / P$ is the magnitude of the reciprocal lattice vector of the lattice with period P. The defining scalar relation governing q-BICs is that the Q-factor for a given magnitude of perturbation δ_0 follows Ref. [10]

$$Q = \frac{C}{\delta_0^2} \tag{8}$$

for some numerically determined constant C. In terms of this constant, α is given by

$$\alpha = \frac{k_g}{2C} \delta_0^2 . \tag{9}$$

Meanwhile, since the Q-factor is the ratio of stored energy to leaked energy, we expect

$$Q = \frac{|A|^2}{|B|^2} = \frac{1}{\beta^2} . \tag{10}$$

Conceptually, β is related to the coupling coefficients $|d\rangle$ in temporal coupled-mode theory, containing phase and polarization information as well as information regarding the Q-factor. Based on our previous investigations [9] we may write:

$$\beta = \frac{\exp(i\delta)}{\sqrt{Q}} = \frac{\delta_0}{\sqrt{C}} \exp(i\delta) \tag{11}$$

where the perturbations 1 and 2 have (signed) magnitudes δ_1 and δ_2, and

$$\begin{aligned} \delta_0 &= \sqrt{\delta_1^2 + \delta_2^2} \\ \delta &= \operatorname{atan2}(\delta_2, \delta_1) \end{aligned} . \tag{12}$$

(Note: δ_i being negative is geometrically equivalent to fixing δ_i to be positive but instead flipping α_i to $\alpha_i + 90°$.)

Next, we allow the perturbation to vary, i.e., characterized by $\delta(y)$ and $\delta_0(y)$. If the magnitude of the perturbation remains small and varies sufficiently slowly, we may approximate our system with:

$$\frac{dA(y)}{dy} = -\frac{k_g}{2C}\delta_0^2(y)A(y) \tag{13}$$

$$B(y) = \frac{\delta_0(y)}{\sqrt{C}}\exp\left[i\delta(y)\right]A(y) \tag{14}$$

As shown in Ref. [11], then for a *desired* outgoing profile $\left|B(y)\right| = G(y)$, the perturbation strength should follow

$$\delta_0(y) = \sqrt{C}\frac{G(y)}{\sqrt{1-\left(1-A_e^2\right)\int_0^y dy' G_N^2(y')}} \tag{15}$$

where A_e is the residual electric field magnitude at the end of the LWM, and

$$G_N(y) = \sqrt{\frac{k_g}{1-A_e^2}}G(y), \tag{16}$$

which is subject to the normalization

$$\int_0^{y_e} dy' G_N^2(y') = 1, \tag{17}$$

where the LWM spans from $y = 0$ to $y = y_e$.

We now numerically explore a few examples involving a Gaussian profile. Here we compute the propagation of the mode in 2D based on the approach detailed in the following section, but we assume that the magnitude of perturbation is invariant in x. In **Fig. S12**, we study a high-efficiency version of the focusing LWM, showing that surface emission with 99% efficiency may be achieved by carefully adjusting $|\beta|$ along the y-direction. To achieve this within a LWM aperture of 1 mm, a peak scattering efficiency of $\beta_{\max} \approx 0.04$ is required, corresponding to a minimal Q-factor of $Q_{\min} \approx 625$. Previous efforts on nonlocal metasurfaces in high-index-contrast systems have shown Q-factors in the low 100s [12], suggesting that this example target device is achievable in similar systems.

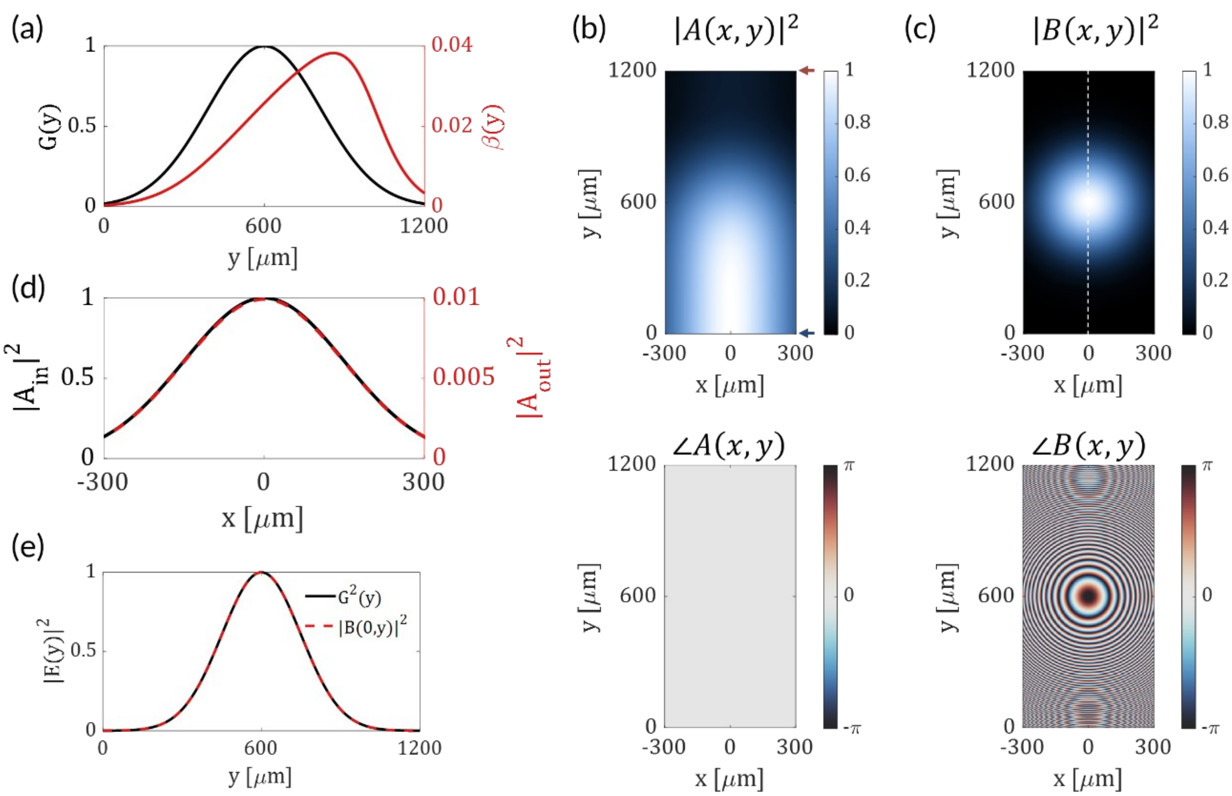

Figure S12. Focusing LWM with high efficiency. (a) Target amplitude profile $G(y)$ and computed profile of scattering magnitude $|\beta(y)|$ required to achieve it with a power efficiency of $1-A_e^2=0.99$. (b) Calculated intensity (top) and phase (bottom) of the guided wave on a discrete grid with a pixel size equal to the effective wavelength of the mode (i.e., corresponding to the mode at the Γ point). (c) Out-coupled wave's intensity (top) and phase (bottom). (d) Input field intensity at the blue arrow in (b) and output field intensity at the red arrow in (b). (e) Comparison of target out-coupled intensity profile $G^2(y)$ and computed out-coupled intensity profile $|B(0,y)|^2$ along the dashed line in (c).

In the low contrast system in the main text, the minimum achievable Q-factor is in the mid $10^4 - 10^5$ range, i.e., at least an order of magnitude higher than that required in **Fig. S12**. This means that for similar-sized LWM apertures, vast majority of the power will stay in the guided mode, and the required perturbation profile will negligibly differ from simply being proportional to the target amplitude profile. This is confirmed in **Fig. S13**, where scattering strengths typical of the devices in the main text are used.

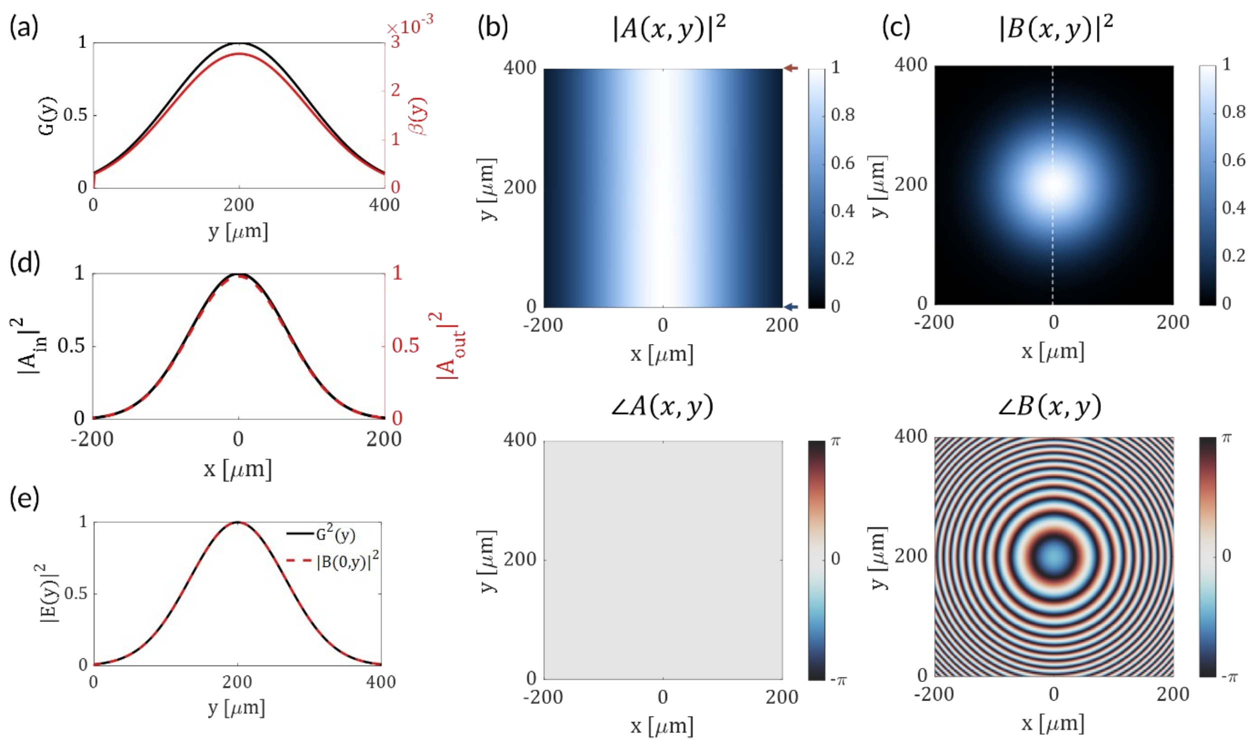

Figure S13. Focusing LWM with low efficiency. (a) Target amplitude profile $G(y)$ and computed profile of scattering magnitude $|\beta(y)|$ required to achieve it with a power efficiency of $1-A_e^2=0.01$. (b) Calculated intensity (top) and phase (bottom) of the guided wave on a discrete grid with a pixel size equal to the effective wavelength of the mode (i.e., corresponding to the mode at the Γ point). (c) Out-coupled wave's intensity (top) and phase (bottom). (d) Input field intensity at the blue arrow in (b) and output field intensity at the red arrow in (b). (e) Comparison of target out-coupled intensity profile $G^2(y)$ and computed outcoupled intensity profile $|B(0,y)|^2$ along the dashed line in (c).

Last, we note that while this section overviewed long-known approaches for apodized grating couplers that vary in one dimension in order to maximize efficiency, recent efforts have also extended these concepts to two-dimensionally varying grating couplers [13].

S.12 Two-dimensional propagation of the leaky wave

When we target a 2D custom emission profile $B(x, y)$, the simplified analysis in the previous section is insufficient. Instead, we must numerically solve the propagation of the guided mode including the effects of its local amplitude being attenuated due to the LWM's scattering. Consistent with the discrete nature of metasurfaces, we discretize the field in the propagation direction, i.e., the field has a complex field amplitude $A_i(x)$ at the i^{th} row of meta-units (spaced with the lattice period P). We keep the x-dependence continuous for conceptual clarity, but in practice it is also discretized.

We begin by assigning an input field $A_0(x) = E_{in}(x)$ at a position $y = -P$, which is propagated to the first row of meta-units by the angular spectrum method, i.e.,

$$A_i^0(x) = \mathcal{F}^{-1}\left\{\mathcal{F}\left\{A_{i-1}(x)\right\}\exp\left(i\sqrt{k_0^2 - k_x^2}P\right)\right\}, \tag{18}$$

where $\mathcal{F}\{\}$ denotes the Fourier transform from x to k_x, k_0 is the wavevector of the guided mode (i.e., $k_0 = k_g$ for the mode at the Γ point), and the superscript 0 denotes that this field has not yet been adjusted by the scatterers at the i^{th} row. Then, the out-coupled field at the i^{th} row is computed by [see Eqn. (7)]:

$$B_i(x) = \beta_i(x) A_i^0(x), \tag{19}$$

while finally, the guided mode's field profile is updated via

$$A_i(x) = A_i^0(x)\left[1 - k_g\left|\beta_i(x)\right|^2 P/2\right], \tag{20}$$

where we have used the relation

$$\alpha = k_g \beta^2 / 2 \,. \tag{21}$$

We next show some numerical examples exploring the downstream effects of the guided mode being continuously attenuated as it propagates. Here, we may include the effects of 2D LWM amplitude profiles. We begin with the two-image hologram in **Fig. 5** of the main text, seen in **Fig. S14**. For five values of a maximal scattering strength $|\beta_{\max}|$, we numerically compute the out-coupled field intensity, $|B(x, y)|^2$, and the guided mode's complex field profile $A(x, y)$, and compare the residual intensity in the guided mode at the end of the LWM and the intensity profile at the beginning. From this study, we can see at the lower scattering strengths, the guided mode is negligibly affected by the minimal attenuation, and the out-coupled field matches well with the desired field. But as the attenuation grows, the mode begins to attenuate, and the out-coupled field's profile deteriorates.

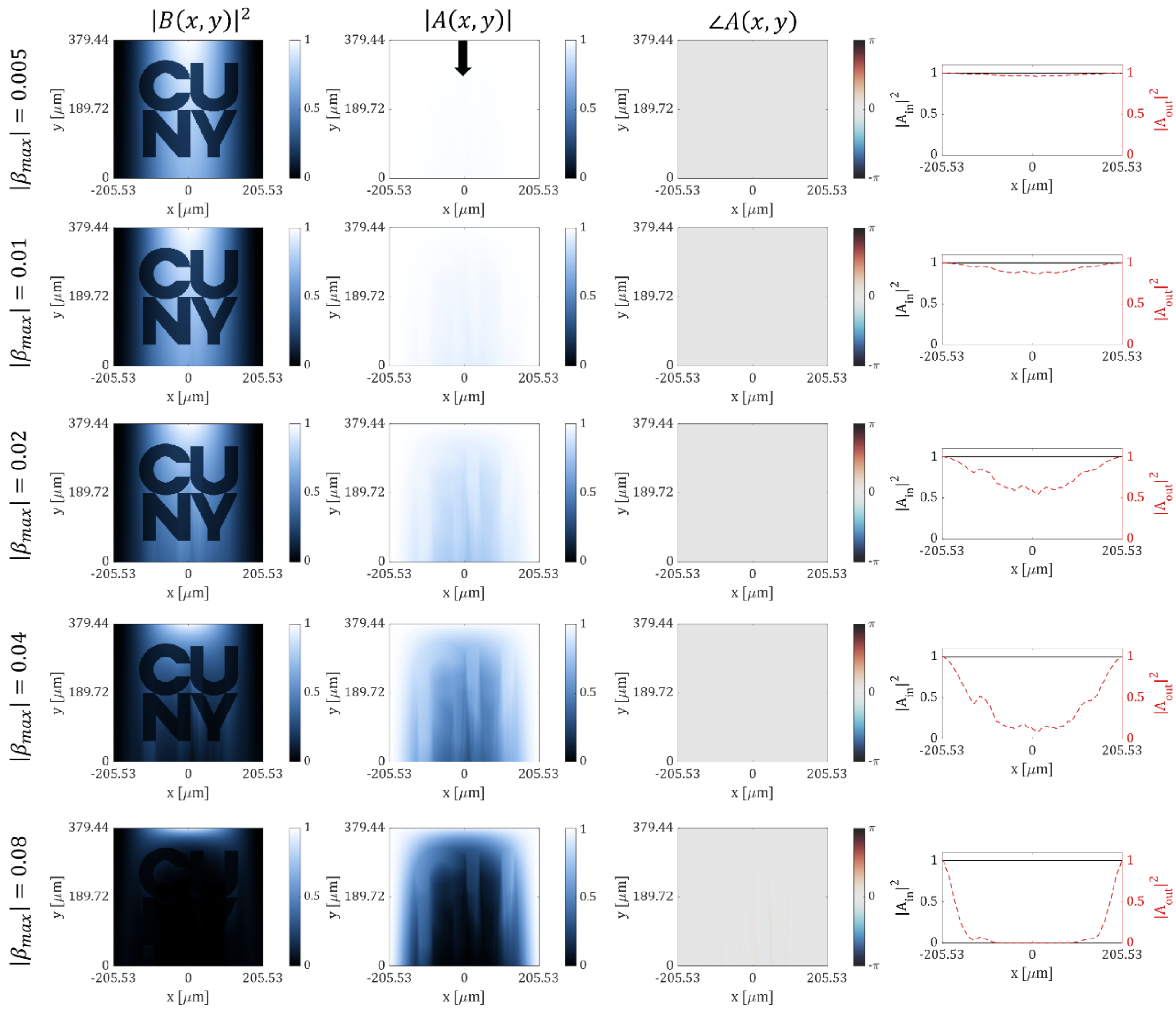

Figure S14. Numerical exploration of the two-image hologram in the main text. (Left to Right) Output scattering intensity profile, guided wave amplitude profile, guided wave phase profile, and cross section of the intensity of the guided wave at the input and output of the LWM. Energy is incident in the $-y$ direction, here, indicated by the black arrow in the top row. The five rows correspond to five values of maximal scattering strength $|\beta_{\max}|$ encoded by the LWM.

Next, as shown in **Fig. S15**, we study an extreme case of x-dependent attenuation, namely, a sinusoidal amplitude variation. Again, at low scattering strengths, most of the guided mode remains in the slab, and the out-coupled field matches well with the target. However, as the attenuation grows, we see not only weakened amplitude of the out-coupled field, but also substantial in-plane scattering of the guided mode. Even in the second row we begin to see interference fringes in the downstream amplitude profile of the guided mode, arising from the guided mode's in-plane diffraction due to the sinusoidal modulation of the scattering strength. In the extreme values of the scattering strength, even the phase of the guided mode has substantial deviations from the input field. These effects on the phase profile of the guided mode are just barely perceptible in the final row of **Fig. S14**, but in **Fig. S15** are much more pronounced due to the large spatial frequency of the attenuation.

From these studies, we see that the 2D profile of the guided mode can be numerically calculated, and that while at low scattering efficiencies the resulting effects may be ignored, at high scattering efficiencies they are non-negligible. Future work may expand on this to maximize the use of the in-plane energy without sacrificing the integrity of the out-coupled field profile. In the present work, the low scattering efficiencies involved require no such adjustments. We note that this simple approach does not account for reflection from the boundaries of the waveguide, nor the dispersion of the lattice having a dependence on the in-plane propagation angle. For simplicity, we also assumed a flat phase profile for the incident guided modes. This, together with operating at the Γ point, means that the "ideal" propagation has a uniform phase profile in $\angle A(x, y)$, since the discrete sampling of the phase has a periodicity precisely equal to that of the guided mode.

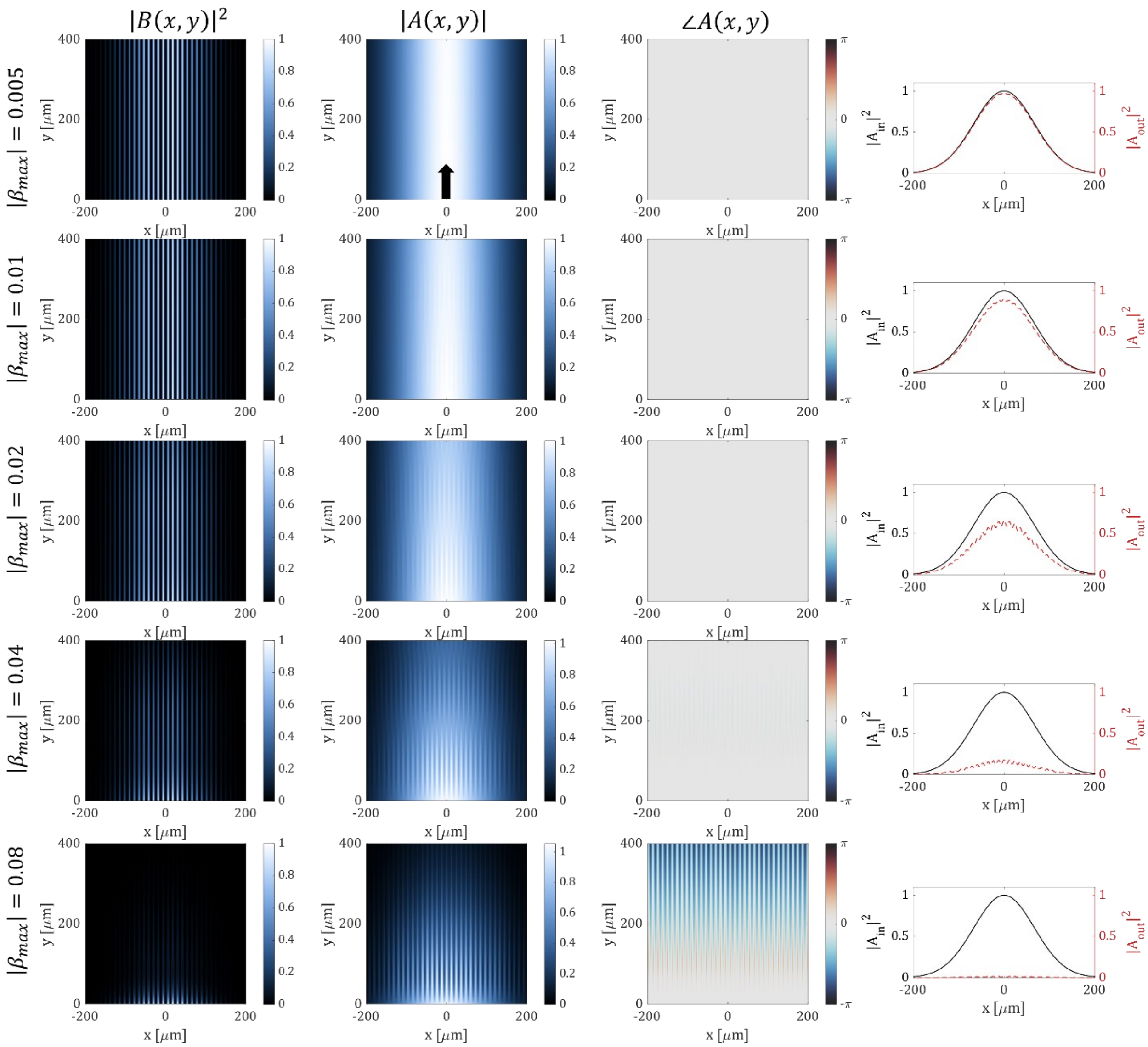

Figure S15. Numerical exploration of a lateral-grating LWM. (Left to Right) Computed output scattering intensity profile, guided wave amplitude profile, guided wave phase profile, and cross section of the intensity of the guided wave at the input and output of the LWM. Energy is incident in the $+y$ direction, here, indicated by the black arrow in the top row. The five rows correspond to five values of maximal scattering strength $|\beta_{\max}|$ encoded by the LWM.

Finally, we note that defects in the fabricated LWM devices can cause in-plane scattering of light, leading to downstream streaks in the surface emission profile, seen in **Fig. S16**. However, unlike the streaks in **Fig. S14**, these can be removable by improved fabrication.

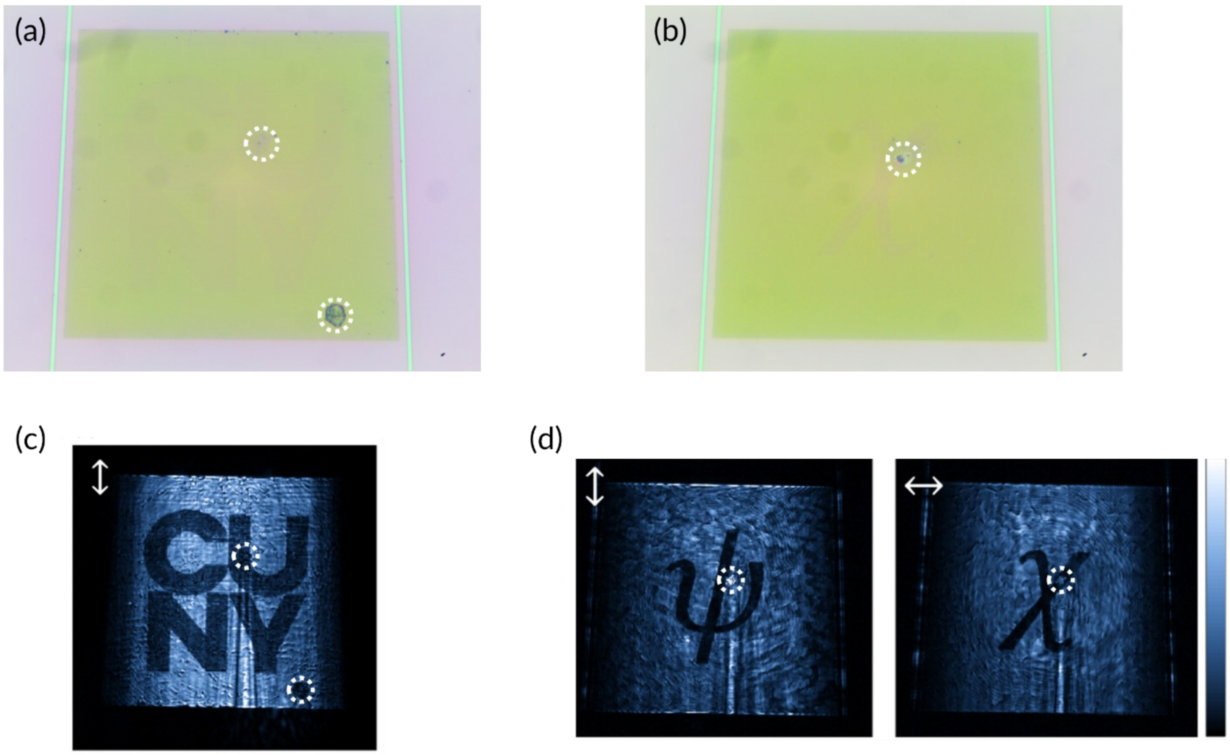

Figure S16. Downstream streaks due to fabrication defects. Optical images of (a) the two-image hologram and (b) four-image hologram of the main text with notable defects circled. (c,d) Experimental results from **Fig. 5** and **Fig. 6** of the main text, showing downstream streaks caused by the defects.

S.13 Improvements and Extensions

We highlight a few improvements that may be explored to further extend the impact of this work. First, while we showed compatibility with large-aperture fields, we made no attempt to optimize the scattering for large radiation efficiency. Future efforts may explore matching the aperture radiation field with the amplitude profile of the quasi-bound wave to optimally utilize the incident guided wave [11],[13]. As discussed in **Supplementary Materials S.11** and **S.12**, in cases *without* transverse amplitude modulation of the slab mode (here, in the x direction), the radiation efficiency may approach unity by properly designing the profile of the perturbation strength in the propagation direction (here, in the y direction). However, in cases *with* lateral amplitude modulation (e.g., holography), in-plane diffraction may result from local depletion of the slab mode as it propagates. In such cases, the evolution of the slab mode's complex profile must be accounted for by adjusting the sign and strength of the perturbation to match the desired output field. Given maximal achievable scattering strength within the meta-unit library, a minimum device length is required to achieve a target device efficiency. In our case, we estimate this length to be several millimeters, putting our devices in the regime where most of the optical power remains within the device. In other words, the complications due to depletion of the slab mode are negligible here, at the cost of low device efficiency.

Second, while in our case the flat band observed in **Fig. 2(i)** did not negatively impact the function of our device, in deeply corrugated structures scattering between the Dirac point and this flat band may introduce unwanted cross-talk. This may be avoided by adjusting the lattice dimensions a_x and a_y (**Supplementary Materials S.3**). Relatedly, while for certain meta-units the Dirac point directly at the Γ point is protected by glide symmetry, in the general case of symmetry-broken meta-units and/or random scattering from fabrication errors, small band gaps or exceptional points [14] may complicate the behavior. For a small range of frequencies (near where the modes cross at the Γ point), the fidelity of the desired responses may suffer in applications requiring extremely collimated light. However, as discussed in **Supplementary Materials S.4**, due to the perturbative nature of our approach as well as the low index contrast of our system, these issues are negligible in our present devices; they are minor even in higher index-contrast silicon-on-insulator systems.

Last, here we limited our operation to near-normal surface emission (with moderate effective numerical apertures in the range of $NA \approx 0.1 - 0.37$), allowing us to decouple the real and imaginary components of the scattered wave via their distinct symmetries. At large NA operation or at extreme deflection angles, this assumption may be invalid, implying that more complex meta-unit design must be taken into account. The origin of this limitation is that, while Perturbation 1 (2) does not introduce a net *dipole* moment to the imaginary (real) part of scattering, it does in general introduce a net *quadrupole* moment (see **Fig. S4**). Near broadside, the dipolar emission dominates, validating our design assumptions, but to varying degrees in different systems, at large angles away from broadside the quadrupole may become comparable in scattering amplitude to the dipole, invalidating our design assumptions. Several extensions may also be explored. First, two-layer devices based on similar period-doubling symmetry-breaking principles have shown exquisite control over the leakage of chiral states [15]. Here, our approach has been primarily achiral: due to the insignificant breaking of out-of-plane symmetry, the upward and downward radiating states are mirror images of each other. In contrast, two-layer devices may add additional control to manipulate separately the upward and downward radiation. Similarly, multi-perturbation devices based on symmetry-breaking have shown control over several leaky waves at distinct frequencies simultaneously [12],[16]. Here, our approach controlled a single mode, but future work may extend the platform to control orthogonally propagating modes (similar to the recent achievements in Ref. [17]). Next, while here we used a weakly corrugated system without deliberate command of the group velocity, band structure engineering (see, e.g., Refs. [18] and [19]) may be used to tune the angular dispersion of the output. Last, while here we implemented a single device layer, due to the broadband transparency of these nonlocal metasurfaces to free-space light, future works may cascade several LWMs at optically thick distances for multi-wavelength operation [12]. Notably, such cascading scheme is not generically compatible with the MOW approach [**Fig. 1(c)**].

Supplementary References

[1] T. Wu, X. Zhang, Q. Xu, E. Plum, K. Chen, Y. Xu, Y. Lu, H. Zhang, Z. Zhang, X. Chen, G. Ren, L. Niu, Z. Tian, J. Han, and W. Zhang, "Dielectric metasurfaces for complete control of phase, amplitude, and polarization," *Advanced Optical Materials* **10**, 2101223 (2022).

[2] M. Liu, W. Zhu, P. Huo, L. Feng, M. Song, C. Zhang, L. Chen, H. J. Lezec, Y. Lu, A. Agrawal, and T. Xu, "Multifunctional metasurfaces enabled by simultaneous and independent control of phase and amplitude for orthogonal polarization states," *Light: Science & Applications* **10**, 107 (2021).

[3] B. Fang, Z. Wang, S. Gao, S. Zhu, and T. Li, “Manipulating guided wave radiation with integrated geometric metasurface,” *Nanophotonics* **11**, 1923–1930 (2022).

[4] Y. Ding, X. Chen, Y. Duan, H. Huang, L. Zhang, S. Chang, X. Guo, and X. Ni, “Metasurface-dressed two-dimensional on-chip waveguide for free-space light field manipulation,” *ACS Photonics* **9**, 398–404 (2022).

[5] Z. Huang, D. L. Marks, and D. R. Smith, “Out-of-plane computer-generated multicolor waveguide holography,” *Optica* **6**, 119–124 (2019).

[6] Y. Ha, Y. Guo, M. Pu, X. Li, X. Ma, Z. Zhang, and X. Luo, “Monolithic-integrated multiplexed devices based on metasurface-driven guided waves,” *Advanced Theory and Simulations* **4**, 2000239 (2021).

[7] Y. Livneh, A. Yaacobi, and M. Orenstein, “Two-dimensional quasi periodic structures for large-scale light out-coupling with amplitude, phase and polarization control,” *Optics Express* **30**, 8425–8435 (2022).

[8] A. C. Overvig, S. C. Malek, M. J. Carter, S. Shrestha, and N. Yu, “Selection rules for quasi-bound states in the continuum,” *Physical Review B* **102**, 035434 (2020).

[9] A. C. Overvig, Y. Kasahara, X. Gu, and A. Alu, “Complete command of scattering in diffractive nonlocal metasurfaces supporting a polarization-agnostic geometric phase,” [Submitted].

[10] K. Koshelev, S. Lepeshov, M. Liue, A. Bogdanov, and Y. Kivshar, “Asymmetric metasurfaces with high-Q resonances governed by bound states in the continuum,” *Physical Review Letters* **121**, 193903 (2018).

[11] K. A. Bates, L. Li, R. L. Roncone, and J. J. Burke, “Gaussian beams from variable groove depth grating couplers in planar waveguides,” *Applied Optics* **32**, 2112–2116 (1993).

[12] S. C. Malek, A. C. Overvig, A. Alu, and N. Yu, “Multifunctional resonant wavefront-shaping meta-optics based on multilayer and multi-perturbation nonlocal metasurfaces,” *Light: Science & Applications* **11**, 246 (2022).

[13] Z. Zhao and S. Fan, “Design principles of apodized grating couplers,” *Journal of Lightwave Technology* **38**, 4435–4446 (2020).

[14] A. Yulaev, S. Kim, Q. Li, D. A. Westly, B. J. Roxworthy, K. Srinivasan, and V. A. Aksyuk, “Exceptional points in lossy media lead to deep polynomial wave penetration with spatially uniform power loss,” *Nature Nanotechnology* **17**, 583-589 (2022).

[15] A. C. Overvig, N. Yu, and A. Alù, “Chiral quasi-bound states in the continuum,” *Physical Review Letters* **126**, 073001 (2020).

[16] A. C. Overvig, S. C. Malek, and N. Yu, “Multifunctional nonlocal metasurfaces,” *Physical Review Letters* **125**, 017402 (2020).

[17] Y. Shi, C. Wan, C. Dai, S. Wan, Y. Liu, C. Zhang, and Z. Li, “On-chip meta-optics for semi-transparent screen display in sync with AR projection,” *Optica* **9**, 670–676 (2022).

[18] R. Magnusson, M. Shokooh-Saremi, and X. Wang, “Dispersion engineering with leaky-mode resonant photonic lattices,” *Optics Express* **18**, 108–116 (2010).

[19] H. S. Nguyen, F. Dubois, T. Deschamps, S. Cueff, A. Pardon, J.-L. Leclercq, C. Seassal, X. Letartre, and P. Viktorovitch, “Symmetry breaking in photonic crystals: on-demand dispersion from flatband to Dirac cones,” *Physical Review Letters* **120**, 066102 (2018).